Center for Turbulence Research
Annual Research Briefs 2018

A computational framework for stability analysis of high-speed flows in complex geometries

By T. Flint and M. J. P. Hack

1. Motivation and objectives

Transition to turbulence plays a central role in the design and performance of hypersonic vehicles. Specifically, heat transfer to the surface can grow by a factor of eight in high-speed boundary layers past the onset of transition (Leyva 2017). Boundary layer transition in high-speed flight still poses a scientific challenge and requires a more thorough understanding of the underlying flow physics. Specifically, the receptivity stage of the transition process that governs the initiation of a perturbation field inside the shear layer by external sources of excitation such as free-stream turbulence remains poorly understood.

Direct numerical simulations (DNS) have advanced the general understanding of the general transition process in high-speed boundary layers. Comprehensive studies by Zhong & Wang (2012) evaluated the influence of different types of upstream conditions on the transition process. More recently, Hader & Fasel (2018) investigated the flow over a flared cone, without however taking into account the effects of shock waves and the leading edge. Input-output analysis has proven successful in explaining complex behavior such as the delay and subsequent enhancement of the growth of instabilities on cones with blunt tips at high speed (Cook *et al.* 2018).

Missing from the literature on high-speed transition is a rigorous receptivity analysis based on the identification of specific external conditions that trigger instabilities such as the second Mack mode. Although the underlying mathematical theory is well developed, computational implementations have been largely limited to low-speed flows.

Global stability and receptivity analysis based on the linearized and adjoint linearized operators provides a means to examine the properties of flow instabilities in the presence complex geometries. The use of adjoint systems to study the receptivity problem was pioneered by Hill (1995). Global analysis has been recently applied to the flow around a swept wing in the incompressible regime (Meneghello *et al.* 2015). This method enabled the study of global modes and identification of regions that are sensitive to external forcing, and regions sensitive to modifications of the base state. Such results are useful in determining where, for example, control should be placed in order to have maximum influence on the flow field (Gianetti & Luchini 2007). In the high-speed regime, a similar method has been used to study the flow around a swept parabolic body (Mack & Schmid 2010), though the influence of shocks was excluded from the analysis. The global analysis of the canonical high-speed cone is yet to be performed.

In the present study, a framework for the global stability and receptivity analysis of high-speed flows involving complex geometry and shocks is presented. The chosen application is that of a blunt cone traveling at hypersonic velocities. The goal is to enable global stability, receptivity, and structural sensitivity analysis that includes the effect of both geometry and shock waves which is yet to be investigated.

In Section 2 of this brief, the governing equations and the concepts of adjoint-based receptivity analysis are introduced, followed by a description of the numerical implementation in Section 3. The flow solver is verified in Section 4 by applying it to two canonical test cases. Preliminary results from the analysis of the flow over a high-speed cone are presented in Section 5 and Section 6 contains final conclusions.

2. Theoretical background

2.1. *Governing equations*

The flow of a compressible, perfect gas in chemical and thermal equilibrium in the continuum regime is considered. In the formulation of the governing equations, the following non-dimensionalization of the primitive dependent variables are used

$$\rho = \frac{\rho^*}{\rho_\infty},\ u_i = \frac{u_i^*}{a_\infty},\ p = \frac{p^*}{\rho_\infty a_\infty^2},\ T = \frac{T^* c_p^*}{a_\infty^2}, \tag{2.1}$$

and for the independent variables

$$x_i = \frac{x_i^*}{l^*},\ t = \frac{t^* a_\infty}{l^*}, \tag{2.2}$$

where $\rho,\ u,\ p,$ and T denote density, velocity, pressure, and temperature, respectively. The superscript $(\cdot)^*$ denotes dimensional quantities, and the subscript $(\cdot)_\infty$ denotes a dimensional ambient quantity. The subscript $(\cdot)_i$ can take a value of 1, 2, or 3 corresponding to components in each of three spatial dimensions. The speed of sound is indicated by a, the specific heat at constant pressure, c_p, and a physical length scale, l^*, which is chosen depending on the problem under consideration.

In three-dimensional Cartesian coordinates, conservation of mass, momentum, and total energy are governed by the compressible Navier-Stokes equations (NSE), in non-dimensional form

$$\frac{\partial \rho}{\partial t} + \frac{\partial \rho u_j}{\partial x_j} = 0, \tag{2.3}$$

$$\frac{\partial m_i}{\partial t} + \frac{\partial m_i u_j}{\partial x_j} = -\frac{\partial p}{\partial x_i} + \frac{\partial \sigma_{ij}}{\partial x_j}, \tag{2.4}$$

$$\frac{\partial e}{\partial t} + \frac{\partial e u_j}{\partial x_j} = -\frac{\partial p u_j}{\partial x_j} - \frac{\partial \iota_j}{\partial x_j} + \frac{\partial \sigma_{jk} u_j}{\partial x_k}, \tag{2.5}$$

where the mass flux, total energy, viscous stress tensor, and heat flux are defined as

$$m_i = \rho u_i, \tag{2.6}$$

$$e = \frac{p}{\gamma - 1} + \frac{1}{2}\rho u_k u_k, \tag{2.7}$$

$$\sigma_{ij} = \frac{\mu}{Re}\left(\frac{\partial u_i}{\partial x_j} + \frac{\partial u_j}{\partial x_i} - \frac{2}{3}\frac{\partial u_k}{\partial x_k}\delta_{ij}\right), \tag{2.8}$$

$$\iota_i = -\frac{\mu}{RePr}\frac{\partial T}{\partial x_i}. \tag{2.9}$$

Here, δ_{ij} refers to the Kronecker delta and $\gamma \equiv c_p/c_v$ is the ratio of the specific heats. The molecular viscosity is non-dimensionalized as $\mu = \mu^*/\mu_\infty$. The Reynolds and Prandtl numbers are defined as

$$Re = \frac{\rho_\infty a_\infty l^*}{\mu_\infty}, \tag{2.10}$$

$$Pr = \frac{c_p^* \mu^*}{\kappa^*}, \tag{2.11}$$

where κ is the thermal conductivity. The Prandtl number is constant under the aforementioned assumptions. The system is closed by the ideal gas equation of state, in non-dimensional form

$$p = \frac{\gamma - 1}{\gamma} \rho T. \tag{2.12}$$

The form of the total energy used here, Eq. (2.7), assumes a perfect gas to relate internal energy, ϵ, to pressure as $\epsilon = p/\left(\gamma - 1\right)$. The dependence of the viscosity on temperature is approximated with a power law, $\mu \sim T^\alpha$, where α is a gas-specific constant. The power-law form is consistent with a hard-sphere model of particle collisions in a gas, though the parameter, α, is empirical and has no physical meaning. The simplicity of the power-law form was favored over the more complex Sutherland law, which includes effects of intermolecular forces though still requires an empirical constant.

2.2. *Linear stability analysis*

In order to study the evolution of small perturbations to the flow field, the dependent variables are decomposed into a base state and a disturbance. In the present study, the transported state variables are chosen to be density, mass flux, and total energy, which are decomposed as follows

$$\mathbf{q} \equiv \begin{bmatrix} \rho \\ m_i \\ e \end{bmatrix} = \begin{bmatrix} \bar{\rho} + \rho' \\ \bar{m}_i + m_i' \\ \bar{e} + e' \end{bmatrix} = \bar{\mathbf{q}} + \mathbf{q}'. \tag{2.13}$$

Here, an overbar, $\bar{(\cdot)}$, indicates the base state and a prime, $(\cdot)'$, indicates the disturbance which is assumed to be of small amplitude. The mass flux disturbance is $m_i' \equiv \bar{\rho} u_i' + \rho' \bar{u}_i$ and the total energy disturbance is $e' \equiv p'/\left(\gamma - 1\right) + \bar{\rho}\bar{u}_k u_k' + \rho' \bar{u}_k \bar{u}_k/2$. Substituting the decomposed field, Eq. (2.13), into the governing equations, Eqs. (2.3) – (2.5), yields the linearized compressible NSE which can be written in vector form as

$$\frac{\partial \mathbf{q}'}{\partial t} + \frac{\partial \mathbf{F}_j'}{\partial x_j} = 0, \tag{2.14}$$

with

$$\mathbf{F}_j' \equiv \begin{bmatrix} \bar{\rho} u_j' + \rho' \bar{u}_j \\ \bar{\rho} \bar{u}_i u_j' + \bar{\rho} u_i' \bar{u}_j + \rho' \bar{u}_i \bar{u}_j + p' \delta_{ij} - \sigma_{ij}' \\ \zeta_j' + \iota_j' + \xi_j' \end{bmatrix} \tag{2.15}$$

and

$$\sigma'_{ij} \equiv \frac{\bar{\mu}}{Re}\left(\frac{\partial u'_i}{\partial x_j} + \frac{\partial u'_j}{\partial x_i} - \frac{2}{3}\frac{\partial u'_k}{\partial x_k}\delta_{ij}\right) + \frac{\mu'}{Re}\left(\frac{\partial \bar{u}_i}{\partial x_j} + \frac{\partial \bar{u}_j}{\partial x_i} - \frac{2}{3}\frac{\partial \bar{u}_k}{\partial x_k}\delta_{ij}\right), \tag{2.16}$$

$$\zeta'_i \equiv \left(\bar{p}u'_i + p'\bar{u}_i\right)\frac{\gamma}{\gamma - 1} + \frac{1}{2}\left(\bar{\rho}\bar{u}_k\bar{u}_k u'_i + 2\bar{\rho}\bar{u}_k u'_k\bar{u}_i + \rho'\bar{u}_k\bar{u}_k\bar{u}_i\right), \tag{2.17}$$

$$\iota'_i \equiv -\frac{\bar{\mu}}{RePr}\frac{\partial T'}{\partial x_i} - \frac{\mu'}{RePr}\frac{\partial T}{\partial x_i}, \tag{2.18}$$

$$\xi'_i \equiv \frac{\bar{\mu}}{Re}\left(\bar{u}_j\frac{\partial u'_j}{\partial x_i} + u'_j\frac{\partial \bar{u}_j}{\partial x_i} + \bar{u}_j\frac{\partial u'_i}{\partial x_j} + u'_j\frac{\partial \bar{u}_i}{\partial x_j} - \frac{2}{3}\left(\bar{u}_j\frac{\partial u'_l}{\partial x_l}\delta_{ij} + u'_j\frac{\partial \bar{u}_l}{\partial x_l}\delta_{ij}\right)\right) \tag{2.19}$$

$$+ 2\frac{\mu'}{Re}\left(\bar{u}_j\frac{\partial \bar{u}_j}{\partial x_i} + \bar{u}_j\frac{\partial \bar{u}_i}{\partial x_j} - \frac{2}{3}\bar{u}_j\frac{\partial \bar{u}_l}{\partial x_l}\delta_{ij}\right). \tag{2.20}$$

Here, μ' is the viscosity perturbation

$$\mu' = \frac{\mathrm{d}\mu}{\mathrm{d}T}T'. \tag{2.21}$$

The linearized equations, Eq. (2.14), can be cast in operator form as

$$\frac{\partial \mathbf{q}'}{\partial t} + \mathsf{L}\mathbf{q}' = 0, \tag{2.22}$$

where L represents the linearized compressible Navier-Stokes equations. For a steady base state, solutions to Eq. (2.22) can be represented as normal modes

$$\mathbf{q}'\left(x_i, t\right) = \hat{\mathbf{q}}\left(x_i\right)\exp\left(-\mathrm{i}\omega t\right). \tag{2.23}$$

Introduction of this ansatz into Eq. (2.22) yields an eigenvalue problem of the form

$$\mathsf{L}\hat{\mathbf{q}} = \mathrm{i}\omega\hat{\mathbf{q}}. \tag{2.24}$$

Here, the eigenvalue, ω, is complex: $\omega = \omega_r + \mathrm{i}\omega_i$. The real part, ω_r, defines the oscillation frequency of the eigenfunction, $f = \omega/2\pi$, and the imaginary part, ω_i, defines the growth rate.

2.3. *Adjoint linearized governing equations*

As a mathematical concept, the adjoint of a linear operator is related to the direct operator through Lagrange's identity (or the generalized Green's theorem if more than one independent variable is used) and provides a tool for solving complex differential equations that are posed as boundary value problems (Morse & Feshbach 1953; Ince 1956). The generalized Green's theorem is

$$\mathbf{u}\mathsf{A}\mathbf{v} - \mathbf{v}\mathsf{A}^{\dagger}\mathbf{u} = \nabla\cdot P\left(\mathbf{u}, \mathbf{v}\right), \tag{2.25}$$

where $\mathbf{u}$ and $\mathbf{v}$ are vector fields, A is a linear operator with $\mathsf{A}^{\dagger}$ its adjoint, and the function, P, is termed the bilinear concomitant. The generalized Green's theorem derives from an extension of Gauss's theorem.

Hill (1995) was among the first to take advantage of the properties of adjoint operators in the context of stability theory and in identifying their relationship to the physical mechanisms by which disturbances in the boundary layer are excited by external means. As will be discussed in Section 2.4, the adjoint field describes the efficiency by which external forcing excites the corresponding eigenfunction.

The adjoint eigenvalue problem is defined as

$$\mathsf{L}^{\dagger}\hat{\mathbf{q}}^{\dagger} = \mathrm{i}\omega^{\star}\hat{\mathbf{q}}^{\dagger}. \tag{2.26}$$

Here, $\hat{\mathbf{q}}^{\dagger}$ is the adjoint eigenfunction to the corresponding direct eigenfunction, $\hat{\mathbf{q}}$, and the eigenvalue, $\omega^{\star}$, is the complex conjugate of that of the direct problem, ω.

2.4. *Adjoint-based receptivity analysis*

The effect of time harmonic forcing on the perturbation field can be accounted for by introducing a source term into the governing equations

$$\frac{\partial \mathbf{q}'}{\partial t} + \mathsf{L}\mathbf{q}' = \mathbf{f}'. \tag{2.27}$$

For the spatial stability problem, Hill (1995) showed that the adjoint eigenfunction, $\hat{\mathbf{q}}^{\dagger}$, acts as a weight on a time-harmonic forcing field, $\hat{\mathbf{f}}$. The streamwise growth in the amplitude of the perturbation eigenfunction, $\hat{\mathbf{q}}$, is obtained as the integral of the projection of the forcing field onto the corresponding adjoint eigenfunction. Hence, for the forcing to most effectively influence the amplitude of the disturbance field, it should be applied in regions where the magnitude of the adjoint eigenfunction is large, which introduces a mathematically rigorous definition of disturbance receptivity. An extension of the adjoint-based receptivity analysis to the temporal problem considered within this work was introduced by Gianetti & Luchini (2007).

3. Computational methodology

3.1. *Overall framework*

The computational framework introduced herein consists of solvers for the time integration of the nonlinear compressible NSE, the linearized NSE, and the adjoint linearized NSE. In addition, the framework also allows the solution of the direct and adjoint eigenvalue problems Eq. (2.24) and (2.26), respectively. Both the linearized and adjoint linearized equations require a base state that is computed by integrating the full NSE, Eqs. (2.3)-(2.5).

3.2. *Nonlinear solver*

The spatial discretization of the nonlinear governing equations, Eqs. (2.3)–(2.5), is based on fourth-order central finite differences. Time integration is facilitated through a fourth-order Runge-Kutta scheme. Complex geometries are treated via a curvilinear formulation invoking the chain rule to evaluate the Cartesian derivatives. The grid metrics are computed to discretely satisfy geometric conservation (Thomas & Lombard 1979), ensuring that a uniform flow field is not affected by the grid topology down to machine precision. Skew-symmetrically split convective terms are used to reduce aliasing errors and spurious contributions to the kinetic energy from the nonlinear terms (Pirozzoli 2011). Boundary conditions are imposed via penalty terms in the governing equations using the simultaneous approximation term (SAT) method (Carpenter *et al.* 1994). Far-field boundaries are enforced with inviscid characteristics to reduce reflections (Svärd *et al.* 2007). The penalties for both far-field and wall boundaries are chosen such that, when used with summation-by-parts (SBP) operators (Strand 1994), the code is provably linearly stable (Svärd & Nordström 2008). In the case of axisymmetric geometry with a coordinate singularity, the axis is treated by shifting grid points to avoid evaluating the governing equations on the axis with differentiation performed through the pole as though it was an internal point (Mohseni & Colonius 2000). Shocks are captured using artificial bulk viscosity, which ensures minimal impact on vortical structures passing through shocks (Mani *et al.* 2009).

In axisymmetric settings, the decrease in azimuthal spacing as the pole is approached introduces a severe time step restriction, owing to the Courant-Friedrichs-Lewy (CFL) condition. The CFL number is defined as

$$CFL = \frac{(u+a)\,\Delta t}{\Delta x} \leq CFL_{max} \tag{3.1}$$

where CFL_{max} is the maximum allowable CFL number for the numerical discretization and Δt is the time step size. The grid spacing, Δx, decreases with radius, r, for a constant azimuthal grid spacing, $\Delta x = r\Delta\theta$. To alleviate this constraint, a sharp spectral filter is applied near the axis to artificially increase the effective azimuthal grid spacing, thereby increasing the allowable time step size (Mohseni & Colonius 2000).

In settings with high cell Reynolds numbers

$$Re_{cell} = \frac{\rho\,(u+a)\,\Delta x}{\mu}, \tag{3.2}$$

stabilization of the numerical scheme is achieved by applying a weak high-frequency compact filter to the simulation domain (Lele 1992). Such a method has been used and validated in many other studies (see Nagarajan 2004).

3.3. *Direct and adjoint linearized governing equations*

The numerical solution of the direct and adjoint linearized NSE is based on the same spatial and temporal discretization as the nonlinear solver. The boundary conditions are imposed using the SAT method with Dirichlet conditions on all boundaries. Owing to the linear nature of the equations, shock capturing is not required.

The linearized NSE were implemented in operator form, Eq. (2.22). Once the direct operators are formed, the adjoint operators are effortlessly implemented by recombining the elements of the direct operator (see Appendix A).

The eigenvalue problems, Eqs. (2.24) and (2.26), arising from the linearized equations are solved using the P_ARPACK (Maschhoff & Sorensen 1996) package, which is based on the implicitly restarted Arnoldi method (Sorensen 1992). In the case when the base state is homogeneous in one dimension (e.g., for an axisymmetric problem), the size of the eigenvalue problem can be significantly reduced by Fourier transforming in the homogeneous direction.

4. Verification

4.1. *Mack vortex*

The implementation of the nonlinear solver includes many elements common to all parts of the present computational framework. To verify the implementation of the nonlinear solver, a mesh convergence study was performed using the compressible Mack vortex (Mack 1960). The setup involves the steady solution of a cylinder rotating in a quiescent fluid. The cylinder has a surface velocity with an equivalent Mach number, Ma_w, and prescribed surface temperature, T_w. Viscosity is assumed to be constant, and an artificial computational boundary is imposed far from the cylinder with the analytic solution prescribed.

Property	Value
Ratio of specific heats, γ	1.4
Prandtl number, Pr	0.71
Wall Mach number, Ma_w	0.2

Table 1. Parameters used in the mesh convergence study based on the Mack vortex.

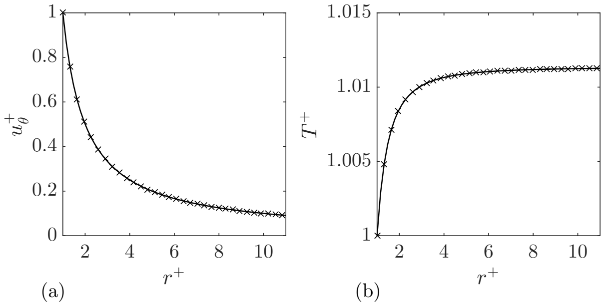

Figure 1. Azimuthal velocity, (a), and temperature, (b), profiles for the Mack vortex test case. Analytic (line) and numerical (symbols) solution.

This case verifies many aspects of the code, most importantly the discretization of the governing equations and the curvilinear formulation. The analytic velocity and temperature profiles are

$$u_\theta^+ = \frac{1}{r^+}, \tag{4.1}$$

$$T^+ = 1 + (\gamma - 1)\, Pr\ Ma_w^2 \left(1 - \frac{1}{{r^+}^2}\right), \tag{4.2}$$

where u_θ is the azimuthal velocity, r is the radius from the center of the domain, and the superscript $(\cdot)^+$ denotes quantities normalized by their values at the surface of the cylinder, $r = R$. The parameters of this mesh convergence study are provided in Table 1.

The velocity and temperature profiles for the Mack vortex test case are shown in Figure 1. Excellent agreement with the analytic solution is observed for both quantities. The results of the mesh convergence study are shown in Figure 2 for both velocity and temperature. The convergence analysis was performed on a uniform grid, so that the number of grid points is inversely proportional to the local grid size. Third-order convergence was achieved, consistent with the expected order when combining fourth-order stencils in the interior of the domain with second-order stencils at the boundaries (Fisher *et al.* 2011).

4.2. *Transient growth in the incompressible pipe*

The time accuracy of the code is verified by applying it to the transient growth of disturbances in incompressible pipe flow. Transient growth is a mechanism by which a superposition of individually decaying eigenfunctions produces energy growth at short times as a result of their non-normality (Schmid & Henningson 1994). After long times, the perturbation energy eventually decays due to viscosity. In incompressible pipe flow

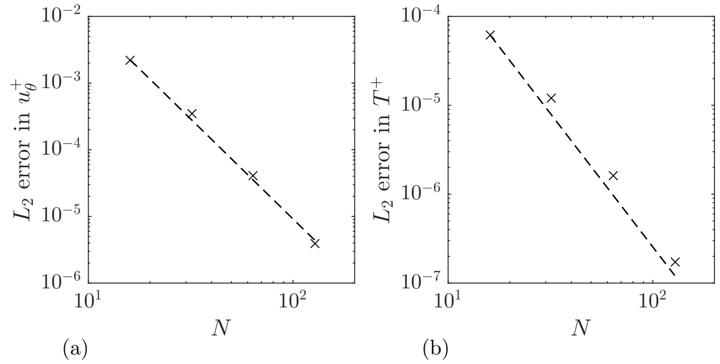

(a) (b)

FIGURE 2. Mack vortex mesh convergence study for (a) azimuthal velocity, and (b) temperature. Third-order convergence (line) and numerical solution (symbols).

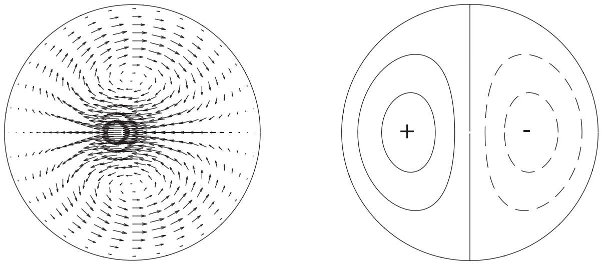

(a) (b)

FIGURE 3. Cross section through pipe. (a) Optimal initial disturbance for transient growth. (b) Contours of the resulting axial velocity perturbation at finite time.

all modes are asymptotically stable, $\omega_i < 0$, implying that perturbation energy growth in the linear regime can only occur through transient growth.

This verification case tests the general implementation of the nonlinear, linearized, and adjoint linearized NSE. The fully compressible formulation used within this work is expected to recover the incompressible solution at sufficiently low Mach number.

Figure 3(a) shows the optimal initial condition which leads to the largest possible energy growth. The initial condition describes two counter-rotating vortices that drive perturbation growth by pulling low-momentum fluid from near the pipe walls on one side toward the center, causing an axial momentum deficit, and pushing high-momentum fluid from the center toward the opposing side, generating an axial momentum surplus, see Figure 3(b).

The reference solution for the transient growth analysis was computed using a spectral discretization of the linearized governing equations in cylindrical coordinates (Hwang & Hack 2018). The parameters used in the compressible solution of the transient growth case are the same as that used in Section 4.1 and are shown in Table 1. The Reynolds number based on the pipe diameter is $Re_D = 4000$. We note that the viscosity is assumed to be constant.

The evolution of the optimal initial condition in time yields the perturbation energy gain, G, shown in Figure 4, where $G(t)$ is defined as the perturbation kinetic energy at

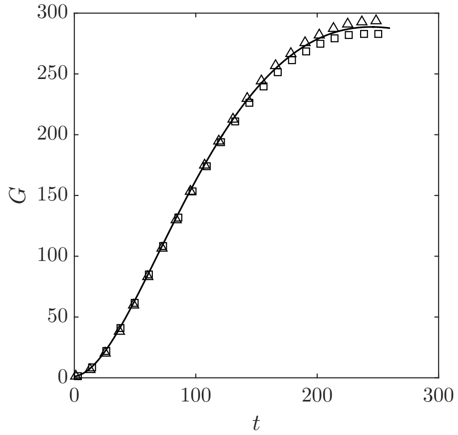

FIGURE 4. Perturbation energy gain, G, with time, t, for pipe flow with the optimal initial condition (Figure 3(a)). Present simulations using the linearized (squares) and nonlinear (triangles) NSE are compared to the incompressible reference solution (line).

time t normalized by its value at the initial time

$$G = \frac{\int_\Omega \rho u_i' u_i' \, \mathrm{d}V|_t}{\int_\Omega \rho u_i' u_i' \, \mathrm{d}V|_{t=0}}. \tag{4.3}$$

Advancing both the linearized and the nonlinear governing equations in time closely recovers the perturbation growth predicted by the reference solution. Discrepancies between the solutions decrease with refinement in time step and mesh resolution. The initial perturbation energy for the nonlinear solver was chosen to be small enough to ensure negligible amplitudes of nonlinear terms.

Initializing the adjoint linearized governing equations with the solution at the time at which the perturbation energy is highest and marching backwards in time is expected to recover the optimal initial condition, scaled by G_{max}^2. The result of marching the adjoint code is shown in Figure 5 and compared to the optimal initial condition. Note that the velocity profiles have been Fourier transformed in the azimuthal direction for comparison

$$u_i = \tilde{u}_i \exp\left(in\theta\right), \tag{4.4}$$

where n is the azimuthal wavenumber ($n = 1$ in this case) and θ is the azimuthal coordinate dimension. The solution marched with the adjoint linearized NSE is seen to accurately recover the initial condition. Note that the oscillations observed in the reference solution in Figure 5(a) are spurious and can be ignored.

5. High-speed flow over a blunt cone

5.1. *Base state*

In the following, the framework presented in Section 3 is applied to the Mach 6 flow over a blunt cone, with certain preliminary results shown in the following. The parameters used in the cone simulation are presented in Table 2. The cone has an isothermal wall with a temperature equal to that of the free-stream temperature, T_∞, effectively making it a cooled wall.

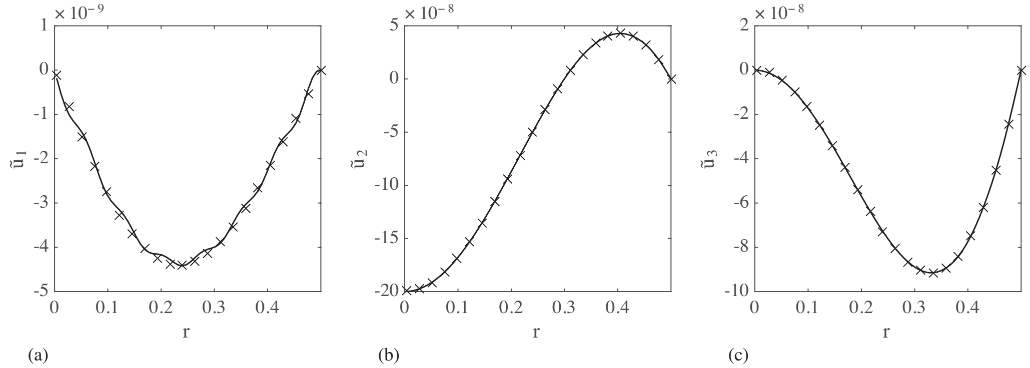

FIGURE 5. Comparison of the azimuthal Fourier coefficients (see Eq. (4.4)) of the optimal transient growth initial condition in a pipe (line) with that recovered by advancing the adjoint linearized governing equations from the state at maximum perturbation energy gain (symbols). (a) Axial velocity, (b) radial velocity, and (c) azimuthal velocity.

Property	Value
Cone half angle, ϕ	7°
Wall temperature, T_w	T_∞
Free stream Mach number, Ma_∞	6
Reynolds number based on tip radius, Re_R	12000
Ratio of specific heats, γ	1.4
Prandtl number, Pr	0.71
Viscosity temperature exponent, α	0.7

TABLE 2. Parameters used for the cone simulation.

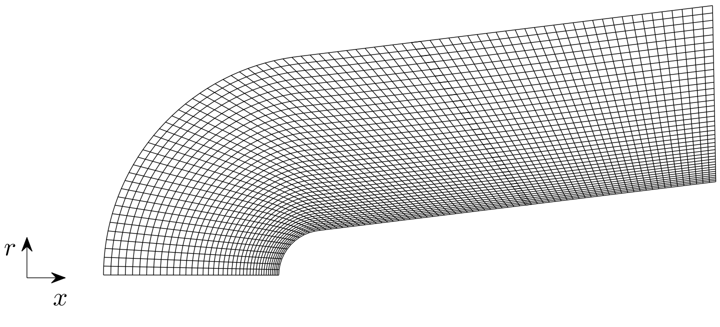

FIGURE 6. Computational mesh used for the blunt cone simulation with the cylindrical coordinate system shown. The mesh is axisymmetric about the x axis. Note that only every 8th row and column are shown to aid visualization.

The axisymmetric computational mesh consists of 320 nodes in the cone-normal direction and 640 nodes in the cone-tangential direction, the structure of which is shown in Figure 6. The mesh is refined toward the cone to resolve the boundary layer using a hyperbolic tangent function. The inflow and outflow boundaries of the domain were treated with characteristic far-field conditions. No-slip boundaries are imposed along the surface of the cone.

FIGURE 7. Contours of the base state axial velocity, $\bar{u}_1$, over a blunt cone at Mach 6. Note the cone is shaded light gray.

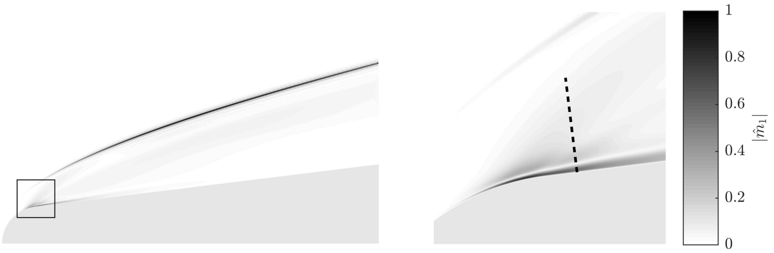

(a) (b)

FIGURE 8. The magnitude of the streamwise mass flux component of the most unstable eigenfunction, $|\hat{m}_1|$, with an azimuthal wavenumber of one. (a) Entire domain. (b) Magnified view of the region near the tip of the cone. The bounds of (b) are indicated by the box in (a). Data in Figure 9 is plotted along the dashed line in (b). The cone is shaded light gray.

Contours of the axial velocity component of the computed base state are shown in Figure 7. The stand-off distance of the bow shock agrees well with the model by Van Dyke (1958) for a parabolic shock over blunt bodies. The shock angle asymptotically approaches ∼14°, as predicted by Maccoll (1937) for inviscid flow over a sharp cone.

5.2. *Most unstable eigenfunction with an azimuthal wavenumber of one*

The eigenvalue problem was solved for the case of an azimuthal wavenumber, n, of one. In the following, viscosity perturbations are neglected, $\mu' = 0$. The most unstable eigenfunction was computed and the magnitude of the streamwise mass flux component is shown in Figure 8. By definition of the eigenfunction, Eq. (2.23), the structure shown in Figure 8 will grow exponentially with time. Apart from a localized region near the shock, this eigenfunction has large magnitude near the tip of the cone, where the geometry transitions from being curved to being straight. The magnitude of the eigenfunction along the dashed line in Figure 8(b) is plotted in Figure 9. While no direct comparison can be made, it is interesting to note that the structure of the eigenfunction at this location qualitatively resembles that of a Tollmien-Schlichting wave as identified in the local analysis of a flat plate boundary layer (see e.g., Schmid & Henningson 2001).

5.3. *Adjoint of the most unstable eigenfunction for an azimuthal wavenumber of one*

The adjoint eigenfunction associated with the direct eigenfunction investigated above is plotted in Figure 10. As discussed in Section 2.4, the adjoint eigenfunction represents

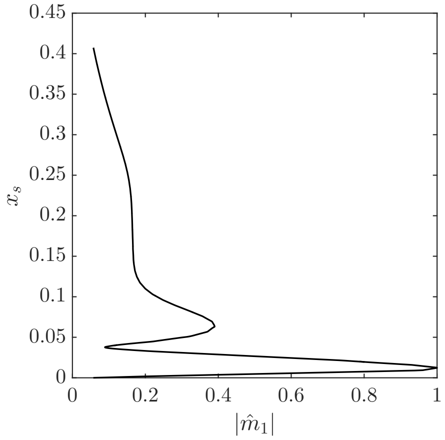

FIGURE 9. The magnitude of the streamwise mass flux component of the most unstable eigenfunction, $|\hat{m}_1|$, plotted along a line, x_s, normal to the surface of the cone near the tip (dashed line in Figure 8). The edge of the boundary layer at this location lies at $x_s \approx 0.1$.

FIGURE 10. Magnitude of the streamwise mass flux component of the adjoint of the most unstable eigenfunction, $|\hat{m}_1^\dagger|$, for an azimuthal wavenumber of one. Note the cone is shaded light gray.

locations in which the corresponding direct eigenfunction is most receptive to forcing. Locations where the magnitude of the eigenfunction is large indicates regions where a small body force would have the most influence on the amplitude of the direct eigenfunction at a later time. The adjoint eigenfunction is confined to a region upstream of the cone bound by diagonal rays, which have a slope corresponding to the free-stream characteristics of the incoming flow. The eigenfunction has its largest magnitude upstream of the bow shock and weakens past the shock and near the surface of the cone.

6. Conclusions

An integrated framework for performing stability analyses of high-speed flows over complex geometry with shock waves has been developed. The framework consists of nonlinear, linearized, and adjoint linearized compressible Navier-Stokes solvers. Eigenvalue problems in the linearized equations are treated with a matrix-free solver. The individual components have been verified in canonical flow configurations, and the complete framework has been applied to high-speed flow over a blunt cone for which preliminary results have been presented. An unstable global eigenfunction of the flow over a high-speed cone was analyzed. The eigenfunction is localized near the curved tip of the cone and shows a profile similar to that of a Tollmien-Schlichting wave. The corresponding adjoint eigenfunction indicates highly receptive regions upstream of the blunt tip and the bow shock, bounded by the incoming free-stream characteristics.

Acknowledgments

This investigation is funded by the Office of Naval Research under Grant #N00014-17-1-2341. The authors would also like to thank Hanul Hwang and Michael Karp for their input and helpful discussions.

Appendix A. Relating the direct and adjoint linearized operators

The adjoint operator, $\mathsf{L}^\dagger$, can be constructed from the direct operator, L. Neither operator is written here for brevity. Recall the linearized governing equations in terms of the perturbation state vector

$$\frac{\partial \mathbf{q}'}{\partial t} + \mathsf{L}\mathbf{q}' = 0, \tag{A 1}$$

which can be rewritten explicitly in terms of each partial derivative of the state vector

$$\begin{aligned}\Bigg(&\mathsf{L}_t\frac{\partial}{\partial t} + \mathsf{L}_0 + \mathsf{L}_{x1}\frac{\partial}{\partial x_1} + \mathsf{L}_{x2}\frac{\partial}{\partial x_2} + \mathsf{L}_{x3}\frac{\partial}{\partial x_3} + \mathsf{L}_{x1x1}\frac{\partial^2}{\partial x_1^2} + \mathsf{L}_{x2x2}\frac{\partial^2}{\partial x_2^2}\\ &+ \mathsf{L}_{x3x3}\frac{\partial^2}{\partial x_3^2} + \mathsf{L}_{x1x2}\frac{\partial^2}{\partial x_1 \partial x_2} + \mathsf{L}_{x1x3}\frac{\partial^2}{\partial x_1 \partial x_3} + \mathsf{L}_{x2x3}\frac{\partial^2}{\partial x_2 \partial x_3}\Bigg)\mathbf{q} = 0.\end{aligned} \tag{A 2}$$

Similarly the adjoint governing equations can be written

$$\begin{aligned}\Bigg(&\mathsf{L}_t^\dagger\frac{\partial}{\partial t} + \mathsf{L}_0^\dagger + \mathsf{L}_{x1}^\dagger\frac{\partial}{\partial x_1} + \mathsf{L}_{x2}^\dagger\frac{\partial}{\partial x_2} + \mathsf{L}_{x3}^\dagger\frac{\partial}{\partial x_3} + \mathsf{L}_{x1x1}^\dagger\frac{\partial^2}{\partial x_1^2} + \mathsf{L}_{x2x2}^\dagger\frac{\partial^2}{\partial x_2^2}\\ &+ \mathsf{L}_{x3x3}^\dagger\frac{\partial^2}{\partial x_3^2} + \mathsf{L}_{x1x2}^\dagger\frac{\partial^2}{\partial x_1 \partial x_2} + \mathsf{L}_{x1x3}^\dagger\frac{\partial^2}{\partial x_1 \partial x_3} + \mathsf{L}_{x2x3}^\dagger\frac{\partial^2}{\partial x_2 \partial x_3}\Bigg)\mathbf{q}^\dagger = 0.\end{aligned} \tag{A 3}$$

Using the definition of the adjoint operator

$$\langle \mathsf{L}\mathbf{q}', \mathbf{q}'^\dagger \rangle_\Omega = \langle \mathbf{q}', \mathsf{L}^\dagger \mathbf{q}'^\dagger \rangle_\Omega, \tag{A 4}$$

where the inner product is defined in terms of a pair of vectors $\mathbf{a}$ and $\mathbf{b}$, as

$$\langle \mathbf{a}, \mathbf{b} \rangle_\Omega = \int_\Omega \mathbf{a}^H \mathbf{b}\ \mathrm{d}V, \tag{A 5}$$

the adjoint operator can be written in terms of the direct operator as

$$\begin{aligned}\mathsf{L}_0^\dagger = \mathsf{L}_0^H &- \frac{\partial \mathsf{L}_t^H}{\partial t} - \frac{\partial \mathsf{L}_{x1}^H}{\partial x_1} - \frac{\partial \mathsf{L}_{x2}^H}{\partial x_2} - \frac{\partial \mathsf{L}_{x3}^H}{\partial x_3} + \frac{\partial^2 \mathsf{L}_{x1x1}^H}{\partial x_1^2} + \frac{\partial^2 \mathsf{L}_{x2x2}^H}{\partial x_2^2},\\ &+ \frac{\partial^2 \mathsf{L}_{x3x3}^H}{\partial x_3^2} + \frac{\partial^2 \mathsf{L}_{x1x2}^H}{\partial x_1 \partial x_2} + \frac{\partial^2 \mathsf{L}_{x1x3}^H}{\partial x_1 \partial x_3} + \frac{\partial^2 \mathsf{L}_{x2x3}^H}{\partial x_2 \partial x_3},\end{aligned} \tag{A 6}$$

$$\mathsf{L}_t^\dagger = -\mathsf{L}_t^H, \tag{A 7}$$

$$\mathsf{L}_{x1}^\dagger = -\mathsf{L}_{x1}^H + 2\frac{\partial \mathsf{L}_{x1x1}^H}{\partial x_1} + \frac{\partial \mathsf{L}_{x1x2}^H}{\partial x_2} + \frac{\partial \mathsf{L}_{x1x3}^H}{\partial x_3}, \tag{A 8}$$

$$\mathsf{L}_{x2}^\dagger = -\mathsf{L}_{x2}^H + 2\frac{\partial \mathsf{L}_{x2x2}^H}{\partial x_2} + \frac{\partial \mathsf{L}_{x1x2}^H}{\partial x_1} + \frac{\partial \mathsf{L}_{x2x3}^H}{\partial x_3}, \tag{A 9}$$

$$\mathsf{L}_{x3}^\dagger = -\mathsf{L}_{x3}^H + 2\frac{\partial \mathsf{L}_{x3x3}^H}{\partial x_3} + \frac{\partial \mathsf{L}_{x1x3}^H}{\partial x_1} + \frac{\partial \mathsf{L}_{x2x3}^H}{\partial x_2}, \tag{A 10}$$

$$\mathsf{L}_{x1x1}^\dagger = \mathsf{L}_{x1x1}^H, \tag{A 11}$$

$$\mathsf{L}_{x2x2}^\dagger = \mathsf{L}_{x2x2}^H, \tag{A 12}$$

$$\mathsf{L}_{x3x3}^\dagger = \mathsf{L}_{x3x3}^H, \tag{A 13}$$

$$\mathsf{L}_{x1x2}^\dagger = \mathsf{L}_{x1x2}^H, \tag{A 14}$$

$$\mathsf{L}_{x1x3}^\dagger = \mathsf{L}_{x1x3}^H, \tag{A 15}$$

$$\mathsf{L}_{x2x3}^\dagger = \mathsf{L}_{x2x3}^H, \tag{A 16}$$

where $(\cdot)^H$ denotes the conjugate transpose. The terms involving the derivatives of parts of the direct operator arise because the direct operator involves partial derivatives that must be expanded using integration by parts in order to compare coefficients and satisfy Eq. (A 4).

REFERENCES

Carpenter, M. H., Gottlieb, D. & Abarbanel, S. 1994 Time-stable boundary conditions for finite-difference schemes solving hyperbolic systems: methodology and application to high-order compact schemes. *J. Comput. Phys.* **111**, 220–236.

Cook, D., Thome, J., Brock, J., Nichols, J. & Candler, G. 2018 Understanding effects of nose-cone bluntness on hypersonic boundary layer transition using input-output analysis. In *2018 AIAA Paper 2018-0378.*.

Fisher, T. C., Carpenter, M. H., Nordström, J., Yamaleev, N. K. & Swanson, R. C. 2011 Discretely conservative finite-difference formulations for nonlinear conservation laws in split form: Theory and boundary conditions. *Tech. Rep.* NASA/TM–2011-217307.

Gianetti, F. & Luchini, P. 2007 Structural sensitivity of the first instability of the cylinder wake. *J. Fluid Mech.* **581**, 167–197.

Hader, C. & Fasel, H. F. 2018 Towards simulating natural transition in hypersonic boundary layers via random inflow disturbances. *J. Fluid Mech.* **847**, R3.

Hill, D. C. 1995 Adjoint systems and their role in the receptivity problem for boundary layers. *J. Fluid Mech.* **292**, 183–204.

Hwang, H. & Hack, M. J. P. 2018 The most effective interface disturbance of a round liquid jet, *Annual Research Briefs*, Center for Turbulence Research, Stanford University.

Ince, E. L. 1956 *Ordinary Differential Equations*. Dover Publications, Inc.

Lele, S. K. 1992 Compact finite difference schemes with spectral-like resolution. *J. Comput. Phys.* **103**, 16–42.

Leyva, I. A. 2017 The relentless pursuit of hypersonic flight. *Phys. Today* **70**, 30–36.

Maccoll, J. W. 1937 The conical shock wave formed by a cone moving at a high speed. *Proc. R. Soc. Lond. A. Math. Phys. Sci.* **159** (898), 459–472.

Mack, C. J. & Schmid, P. J. 2010 A preconditioned Krylov technique for global hydrodynamic stability analysis of large-scale compressible flows. *J. Comput. Phys.* **229**, 541–560.

Mack, L. M. 1960 The compressible viscous heat-conducting vortex. *J. Fluid Mech.* **8**, 284–292.

Mani, A., Larsson, J. & Moin, P. 2009 Suitability of artificial bulk viscosity for large-eddy simulation of turbulent flows with shocks. *J. Comput. Phys.* **228**, 7368–7374.

Maschhoff, K. J. & Sorensen, D. C. 1996 P_ARPACK: An efficient portable large scale eigenvalue package for distributed memory parallel architectures. In *Applied Parallel Computing Industrial Computation and Optimization. Lecture Notes in Computer Science* (ed. J. Waśniewski, J. Dongarra, K. Madsen & D. Olesen), vol. 1184. Berlin, Heidelberg: Springer.

Meneghello, G., Schmid, P. J. & Huerre, P. 2015 Receptivity and sensitivity of the leading-edge boundary layer of a swept wing. *J. Fluid Mech.* **775**, R1.

Mohseni, K. & Colonius, T. 2000 Numerical treatment of polar coordinate singularities. *J. Comput. Phys.* **157**, 787–795.

Morse, P. M. & Feshbach, H. 1953 *Methods of Theroetical Physics*. McGraw-Hill.

Nagarajan, S. 2004 Leading edge effects in bypass transition. PhD thesis, Stanford University.

Pirozzoli, S. 2011 Stabilized non-dissipative approximations of Euler equations in generalized curvilinear coordinates. *J. Comput. Phys.* **230**, 2997–3014.

Schmid, P. J. & Henningson, D. S. 1994 Optimal energy density growth in Hagen-Poiseuille flow. *J. Fluid Mech.* **277**, 197–225.

Schmid, P. J. & Henningson, D. S. 2001 Stability and Transition in Shear Flows. Springer.

Sorensen, D. C. 1992 Implicit application of polynomial filters in a k-step Arnoldi method. *SIAM J. Matrix Anal. Appl.* **13**, 357–385.

Strand, B. 1994 Summation by parts for finite difference approximations for d/dx. *J. Comput. Phys.* **110**, 47–67.

Svärd, M., Carpenter, M. H. & Nordström, J. 2007 A stable high-order finite difference scheme for the compressible Navier-Stokes equations, far-field boundary conditions. *J. Comput. Phys.* **225**, 1020–1038.

Svärd, M. & Nordström, J. 2008 A stable high-order finite difference scheme for the compressible Navier-Stokes equations. No-slip wall boundary conditions. *J. Comput. Phys.* **227**, 4805–4824.

Thomas, P. D. & Lombard, C. K. 1979 Geometric conservation law and its application to flow computations on moving grids. *AIAA J.* **17**, 1030–1037.

Van Dyke, M. D. 1958 A model of supersonic flow past blunt axisymmetric bodies, with application to Chester's solution. *J. Fluid Mech.* **3**, 515–522.

Zhong, X. & Wang, X. 2012 Direct numerical simulation on the receptivity, instability, and transition of hypersonic boundary layers. *Annu. Rev. Fluid Mech.* **44**, 527–561.